analytical chemistry

pubs.acs.org/ac Article

Highly Selective Dual-Modal Probe for Photoacoustic and Magnetic Resonance Imaging of the Labile Cu^{2+} Pool in the Liver

Zhaoqing Liu,‖ Lei Zhang,‖ Sha Li, Long Xiao, Qiao Yu, Yue Zhu, Yingying Luo, Maosong Qiu, Xin Zhou, and Shizhen Chen*

Cite This: https://doi.org/10.1021/acs.analchem.5c03093 Read Online

ACCESS | Metrics & More | Article Recommendations | Supporting Information

ABSTRACT: Copper ions (Cu^{2+}) play vital roles in human physiology, and their dyshomeostasis is associated with diseases such as hepatocellular carcinoma, Alzheimer's disease, and Wilson's disease. Cu^{2+} imaging technologies facilitate the investigation of Cu^{2+} dynamics in biological systems. However, developing highly selective and sensitive Cu^{2+} probes that can overcome interference from physiologically abundant Zn^{2+} remains a key challenge. In this study, we design and synthesize a Cu^{2+}-activated dual-modal probe (**BHGd**) for photoacoustic (PA) and magnetic resonance (MR) imaging, which exhibits remarkable specificity for Cu^{2+}. Impressively, **BHGd** demonstrates exceptional selectivity for Cu^{2+} even in the presence of a 1000-fold excess of Zn^{2+}. **BHGd** binds Cu^{2+} in a 1:1 stoichiometry, forming a stable ternary complex in the presence of human serum albumin (HSA), which enhances PA signals by 5.9-fold and increases longitudinal relaxivity (r_1) by 114.9%. Furthermore, *in vivo* experiments demonstrate that **BHGd** enables precise monitoring of labile Cu^{2+} fluctuations in the liver of mice, achieving a remarkable 59% increase in PA signal intensity and a 30% enhancement in MR signal contrast. The systematic investigation demonstrates that **BHGd** can serve as a powerful molecular probe for investigating copper metabolism in living systems. Our breakthrough addresses the long-standing challenge of Cu^{2+}/Zn^{2+} discrimination and provides a design principle for next-generation metal ion probes, with significant potential for diagnosing Cu^{2+} imbalance-related disorders, monitoring therapeutic responses, and advancing biomedical research.

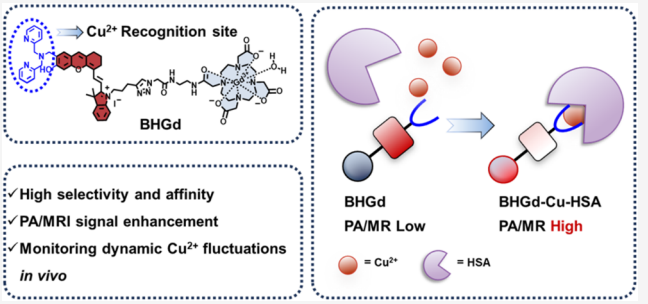

INTRODUCTION

Copper is an essential metal in the human body, serving as a redox-active cofactor in various physiological processes, including energy production, neurotransmitter synthesis and metabolism, gene expression, brain development, and immune system regulation.[1−3] In biological environments, copper primarily exists in two oxidation states: cuprous ion (Cu^{+}) and cupric ion (Cu^{2+}).[4−6] However, the redox-active nature of copper renders it potentially cytotoxic, thereby requiring stringent intracellular homeostatic control to mitigate oxidative stress and free radical-induced damage.[4] Moreover, disruptions in copper homeostasis are associated with various neurodegenerative diseases and metabolic disorders, including Menkes disease,[7] Wilson's disease,[8] familial amyotrophic lateral sclerosis, Alzheimer's disease, and prion diseases.[9,10] Although the homeostasis of Cu^{2+} and physiological consequences of its dysregulation have been extensively studied,[6,10] its specific functional roles in various tissues remain largely elusive, primarily due to the lack of real-time, noninvasive imaging techniques for Cu^{2+} in living systems.

So far, single-modal probes for Cu^{2+} detection have been extensively reported.[11−14] Wang et al. developed a peptide-based biosensor by synthesizing a peptide to mimic the Cu^{2+}-binding sites on bovine serum albumin. This sensor enables continuous monitoring of Cu^{2+} via fluorescence and colorimetric methods and has been successfully applied to imaging Cu^{2+} in live cells and zebrafish models.[15] Expanding beyond optical imaging, Chang and colleagues developed a Cu^{2+}-sensitive MR probe with high selectivity by conjugating a Gd^{3+} complex to an iminodiacetate-Cu^{2+} binding site. Cu^{2+}-binding increased r_1 from 3.76 to 5.29 mM^{-1} s^{-1}. The process was reversible, as excess ethylenediaminetetraacetic acid (EDTA) restored the r_1 signal, demonstrating excellent Cu^{2+} selectivity.[16] Similarly, Sherry and co-workers designed the probe **GdL1**, which exhibits high selectivity for Cu^{2+} with a 43% increase in r_1. The T_1-weighted imaging confirms its capability for *in vivo* Cu^{2+} detection, offering a potential tool for studying Cu^{2+}-related neurological disorders such as Wilson's disease.[17] However, developing single-modal probes

Received: May 29, 2025
Revised: July 28, 2025
Accepted: August 13, 2025

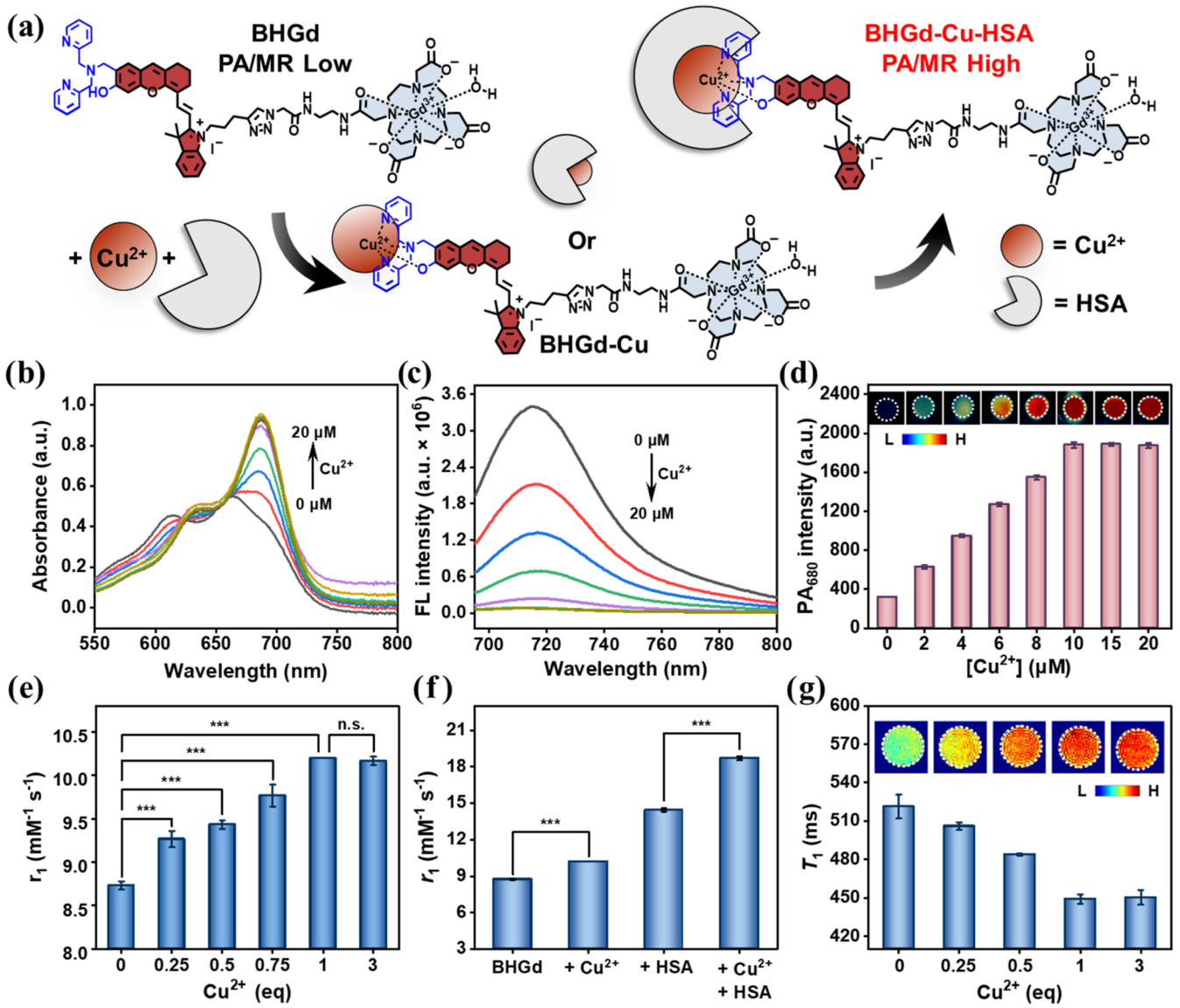

Figure 1. (a) Schematic illustration of the binding mechanism of **BHGd** with Cu^{2+} and HSA. (b) UV−vis absorption spectra and (c) the fluorescence response of **BHGd** (10 μM) upon treatment with Cu^{2+} (0−20 μM). (d) PA signal intensity changes of **BHGd** (10 μM) upon treatment with Cu^{2+} (0−20 μM) under the excitation of 680 nm. (e) Dependence of the r_1 of **BHGd** on Cu^{2+} concentration. (f) Changes in r_1 of **BHGd** in the presence of 1 eq of Cu^{2+}, 0.6 mM HSA, and 1 eq of Cu^{2+} plus 0.6 mM HSA (20 MHz, 37 °C, 0.1 M HEPES buffer, pH 7.4). (g) The T_1 change and phantom images (insert) of **BHGd** (0.3 mM) were acquired at 9.4 T with varying molar concentrations of Cu^{2+} in the presence of 0.6 mM HSA in 0.1 M HEPES buffer. Data are presented as mean ± SD (n = 3), ***P < 0.001 and n.s., P > 0.05.

for Cu^{2+} *in vivo* remains significantly challenging, primarily due to the following aspects. First, while optical imaging achieves exceptional molecular sensitivity, its clinical utility is constrained by limited tissue penetration depth.[18,19] Second, MR imaging of Cu^{2+} can provide unparalleled deep-tissue anatomical resolution but faces two fundamental challenges: (i) the low concentration of free Cu^{2+} in biological systems necessitates the use of contrast agents with strong "turn-on" responses.[20] (ii) The Cu^{2+}-activated probe must have high selectivity and a sufficiently strong affinity for Cu^{2+} to prevent interference from millimolar concentrations of endogenous Zn^{2+}.[17,20,21] The strategic integration of multimodal imaging enables comprehensive copper mapping, bridging subcellular dynamics with organ-level distribution and enhancing diagnostic precision.[22−25] Such dual-modal probes not only monitor labile Cu^{2+} pools with high spatiotemporal resolution but also advance the study of copper dysregulation mechanisms in diseases like Alzheimer's and Wilson's disease.

To address these issues, a PA/MR dual-enhanced probe (**BHGd**) was developed for highly selective and sensitive detection of labile Cu^{2+} pools using PA and MR imaging (Figure 1a). **BHGd** could rapidly and selectively respond to Cu^{2+} with a 1:1 stoichiometry, retaining excellent specificity even in the presence of a 1000-fold excess of Zn^{2+}. Cu^{2+} coordination induces a red-shift in NIR absorption (from 662 to 680 nm) and quenches fluorescence at 718 nm, thereby enhancing photothermal conversion and amplifying the PA signal.[26] Under physiological conditions, **BHGd** could bind with Cu^{2+} and further form a stable ternary complex with HSA, resulting in an "on" state that enhances its MR signal. Owing to its excellent cell permeability and low cytotoxicity, **BHGd** was successfully applied to dynamically monitor labile Cu^{2+} in

https://doi.org/10.1021/acs.analchem.5c03093
Anal. Chem. XXXX, XXX, XXX−XXX

mouse liver via PA and MR imaging. This study presents the design of a Cu^{2+}-specific dual-modal probe with exceptional selectivity, enabling real-time tracking of labile copper pools *in vivo* and providing a transformative strategy for the early diagnosis of disorders associated with copper homeostasis.

EXPERIMENTAL SECTION

Synthesis of BHGd. The chemical structure of **BHGd** comprises three units: (1) a Cu^{2+}-chelating group **BPA**; (2) a near-infrared fluorescent chromophore that functions as a PA signal source while exhibiting minimal background interference; and (3) a paramagnetic **Gd-DO3A** complex for MR imaging applications, enhancing **BHGd's** hydrophilicity and stability for biomedical applications. The synthesis procedures of compounds **Hd-BPA** and **Gd-DO3A-N_3** were described in the Supporting Information (Scheme S1).[22,27] The mixture of compound **Gd-DO3A-N_3** (210.0 mg, 306.5 μmol), compound **Hd-BPA** (266.6 mg, 344.1 μmol), $CuSO_4$ (80.9 mg, 505.6 μmol), ascorbic acid (100.2 mg, 505.6 μmol), *N*,*N*-Dimethylformamide (DMF, 10 mL), and H_2O (1 mL) were stirred at room temperature for 6 h. Then, 2,2′:6′,2″-terpyridine (353.8 mg, 1.5 mmol) in DMF (2 mL) was added to the reaction mixture, followed by an additional 6 h of stirring. The reaction mixture was then evaporated under reduced pressure. The reaction mixture was purified and characterized using high-performance liquid chromatography (HPLC) and high-resolution mass spectrometry (HRMS), affording BHGd as a blue solid (15.0 mg, 3%). HRMS (ESI) Calcd for $C_{63}H_{75}GdIN_{13}O_{10}$, $[M - I + H]^{2+}/2$: 666.2536, Found: 666.2395 (Figure S2).

Cu^{2+} Detection and Selectivity Assay Using BHGd. Stock solutions of metal ions (1.0 mM) and **BHGd** (1.0 mM) were prepared in H_2O. For Cu^{2+} sensing, varying concentrations of Cu^{2+} stock solution were added to **BHGd** to achieve final concentrations of **BHGd** (10.0 μM) and Cu^{2+} (0, 2, 4, 6, 8, 10, 12, 16, and 20 μM) in 0.1 M 4-(2-hydroxyethyl)-1-piperazineethanesulfonic acid buffer (HEPES buffer, pH 7.4). The solutions were incubated at room temperature for 10 min (min), and UV absorption was measured using an Evolution-220 UV−vis spectrometer. Fluorescence spectra were recorded on an Edinburgh FS5 spectrometer with 680 nm excitation. For selectivity experiments, metal ions (Mg^{2+}, Ca^{2+}, Fe^{3+}, Zn^{2+}, Co^{2+}, Ni^{2+}, Mn^{2+}, K^+, Na^+, and Cu^{2+}) were added to **BHGd** (10.0 μM), and the solutions were incubated at room temperature for 10 min. PA imaging was subsequently recorded at a wavelength of 680 nm.

Competing Study Using MR Relaxometer. The r_1 values were measured by a series of inversion-prepared fast spin−echo scans on the 20 MHz MR relaxometer (Niumag, China). The values were determined from the slope of the $1/T_1$ versus **BHGd** concentration plot. Various solutions with different concentrations of **BHGd** (0.05, 0.1, 0.2, and 0.3 mM) complexes were prepared in 0.1 M HEPES buffer (pH 7.4) or in buffer containing 0.6 mM HSA. The solutions of Mg^{2+}, Ca^{2+}, Fe^{3+}, Zn^{2+}, Co^{2+}, Ni^{2+}, Mn^{2+}, K^+, Na^+, and Cu^{2+} were then added to each of the above solutions to obtain the desired $[M^{n+}]$:[**BHGd**] ratios for titrations. The solutions were incubated at a room temperature for 10 min. T_1 measurements were conducted under the same temperature conditions, with warm air blown over the sample to maintain stability.

T_1 MR Imaging of BHGd to Cu^{2+}. The **BHGd** solution (0.3 mM) was prepared in 0.1 M HEPES buffer containing 0.6 mM HSA, and an equimolar amount of Mg^{2+}, Ca^{2+}, Fe^{3+}, Zn^{2+}, and Cu^{2+} was then added to each solution to prepare the sample solutions. These samples were incubated at room temperature for 10 min. T_1 MR imaging was performed using a 9.4 T MR scanner (Bruker, Germany) with a T_1-RAREVTR pulse sequence, with an echo time (TE) of 6 ms and TR values ranging from 100 to 3000 ms.

PA and MR Imaging of Cu^{2+} in Living Cells. Michigan cancer foundation-10A (MCF-10A) cells (1×10^5) were seeded in 3 mL dulbecco's modified eagle medium (DMEM) with 10% fetal bovine serum (FBS) and incubated at 37 °C for 24 h. For PA imaging, cells were treated with Cu^{2+} (40 μM in FBS-free DMEM) for 2 h, then washed with phosphate-buffered saline (PBS) and incubated with 3 mL of **BHGd** (20 μM in DMEM) for 6 h at 37 °C with 5% CO_2. For chelation, elesclomol (TETA, 40 μM in FBS-free DMEM) was added before **BHGd**. After washing with PBS, cells were resuspended in 300 μL PBS and subjected to PA imaging using the MSOT inVision 256-TF system (Germany).

For MR imaging, cells were incubated with Cu^{2+} (120 μM in FBS-free DMEM) for 2 h, followed by washing and incubation with **BHGd** (60 μM in DMEM) for 6 h at 37 °C with 5% CO_2. TETA (120 μM) was added for chelation experiment. After washing with PBS, cells were resuspended in 500 μL PBS and analyzed on a 9.4 T MR scanner (Bruker, Germany) using the T_1-RARE sequence (TE = 5.5 ms, TR = 600.0 ms).

PA and MR Imaging of the Labile Cu^{2+} Pool in Mice. For PA imaging, BALB/c mice were injected with **BHGd** (100 μL, 500 μM) or **BHGd** (100 μL, 500 μM) following ATN-224-treated group (5 mg/kg in 50 μL), with ATN-224 intraperitoneally administered 2 h prior to **BHGd** injection. Liver signal acquisition was performed before injection, followed by manual liver segmentation to quantify mean signal intensities (SI). The percentage signal enhancement (%SE) was calculated using the formula: $\%SE(t) = (SI(t) - SI_0)/SI_0$, where SI_0 represents the preinjection signal intensity.

For T_1-weighted MR imaging, mice were injected with **BHGd** (150 μL, 3.75 mM) or **BHGd** (150 μL, 3.75 mM) following pretreatment with ATN-224 (5 mg/kg in 50 μL), with ATN-224 administered 2 h prior to **BHGd** injection. Mice underwent liver scans before injection and after injection using a 9.4 T MR scanner (Bruker, Germany). During imaging, the mice were positioned tail-first in a prone position under isoflurane anesthesia. Imaging parameters were set as follows: TE/TR = 6:600 ms, image resolution = 256 × 256, slice thickness = 0.8 mm, number of slices = 12, field of view = 35 × 35 mm, and total acquisition time = 10 min 55 s. Liver segmentation was performed manually, and mean signal intensity (SI) values were normalized using a water reference standard to correct for intersession variability. The normalized values were used to calculate mean liver SI at each time point, and %SE was determined using the same formula as in PA imaging.

RESULTS AND DISCUSSION

***In Vitro* Study of Optical and MR Properties of BHGd to Cu^{2+}.** Initially, the optical properties of **BHGd** were investigated using UV−vis absorption, fluorescence emission, and PA imaging. UV−vis spectroscopy results showed that **BHGd** initially exhibited two characteristic absorption peaks at 625 and 662 nm (Figure 1b). Upon the addition of Cu^{2+}, a new absorption peak appeared at 680 nm, exhibiting a clear linear relationship with Cu^{2+} concentration (Figure S3). Additionally, the fluorescence emission of **BHGd** was nearly

https://doi.org/10.1021/acs.analchem.5c03093
Anal. Chem. XXXX, XXX, XXX−XXX

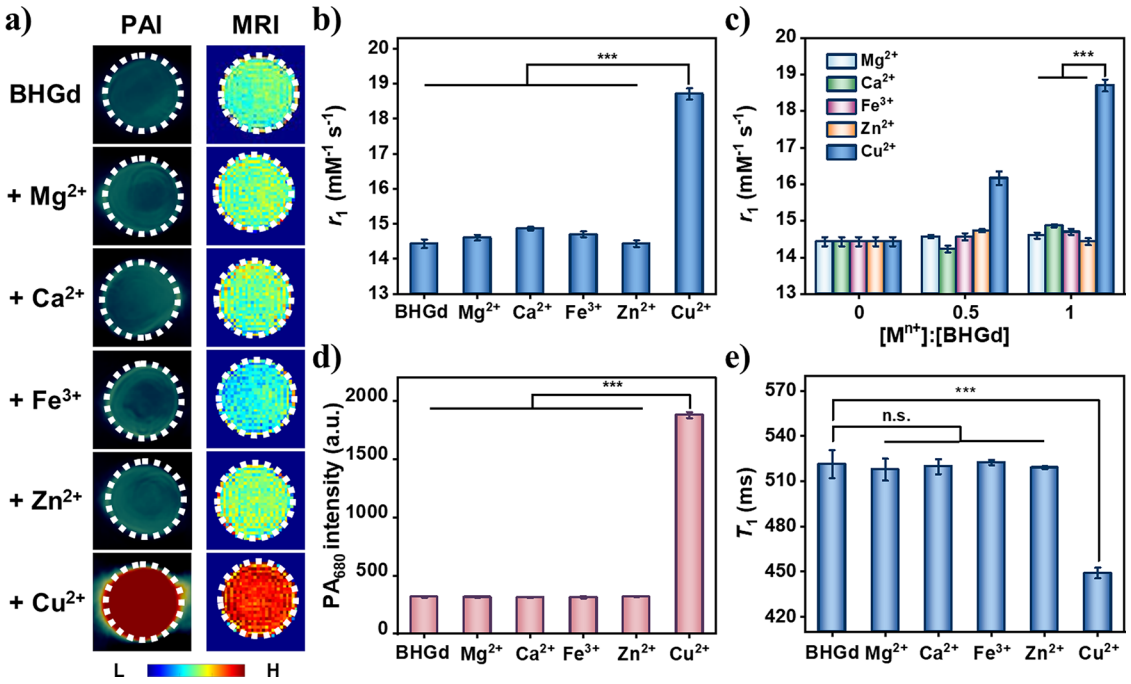

Figure 2. (a) PA imaging (left) of **BHGd** (10 μM) with equimolar concentrations of various metal ions, and corresponding T_1 weighted images (right) of phantoms containing **BHGd** (0.3 mM) with equimolar concentration of various metal ions in the presence of HSA (0.6 mM). (b) The r_1 of **BHGd** with an equimolar amount of M^{n+} plus 0.6 mM HSA and (c) variation of r_1 for **BHGd** with increasing molar eq of M^{n+}, in the presence of 0.6 mM HSA, measured at 20 MHz and 37 °C. (d) Quantitative PA imaging analysis of **BHGd** (10 μM) in the presence of equimolar concentration of metal ions. (e) T_1 weighted image analysis of **BHGd** (0.3 mM) in the presence of equimolar concentration of metal ions in the presence of HSA (0.6 mM). All solutions were prepared in 0.1 M HEPES buffer (pH 7.4). T_1 weighted images were acquired at 9.4 T and room temperature using a T_1-RAREVTR pulse sequence with TE of 6 ms and TR values ranging from 100 to 3000 ms. Data are presented as mean ± SD (n = 3), ***P < 0.001 and n.s., P > 0.05.

quenched at 718 nm (Figure 1c). The dissociation constant (K_d) was determined to be 9.6 μM, demonstrating a strong binding affinity between **BHGd** and Cu^{2+} (Figure S4). Both UV−vis and fluorescence spectra confirmed the equimolar complexation of **BHGd** with Cu^{2+} (Figure S5), which was further confirmed by HRMS (Figure S2). The interaction of **BHGd** with Cu^{2+} was further monitored by PA imaging. As depicted in Figure 1d, **BHGd** alone exhibited a negligible PA signal. However, upon the addition of Cu^{2+}, the PA signal was progressively enhanced. A 5.9-fold increase in signal intensity was observed at equimolar concentrations of **BHGd** and Cu^{2+}. Furthermore, a strong linear correlation was observed between PA intensity and Cu^{2+} concentration in the range of 0−10 μM, with a detection limit of 1.1 × 10^{-7} M (Figure S6).

Next, the regulation of the r_1 of **BHGd** in response to Cu^{2+} was investigated through T_1 value measurements using a 20 MHz relaxometer at 37 °C. As shown in Figure 1e, the r_1 of **BHGd** was at 8.73 ± 0.05 mM^{-1} s^{-1} in the absence of Cu^{2+}. Upon the addition of varying concentrations of Cu^{2+}, the r_1 showed a modest increase, rising to 10.2 mM^{-1} s^{-1} in the presence of one equivalent (eq) of Cu^{2+} and then reaching a plateau. This phenomenon may be attributed to the paramagnetic nature of Cu^{2+} and longer molecular rotational correlation time (τ_R) upon its binding to Cu^{2+}.[17,28,29] It is noteworthy that Cu^{2+} typically binds to proteins and enzymes, playing essential roles in catalysis and structural stabilization.[30,31] As the most abundant protein in human serum, HSA plays a critical role in binding and transporting metal ions, fatty acids, and small molecules. HSA possesses two Cu^{2+} binding sites: a high-affinity N-terminal site (~1 pM) and a lower-affinity multimetal binding site (~10 nM).[32,33] Studies by Sherry's group have shown that Zn^{2+}/Cu^{2+} can be effectively chelated by Zn^{2+}/Cu^{2+}-responsive MR imaging agents, forming binary complexes that subsequently bind to serum albumin, leading to the formation of ternary complexes.[21,34−36] This enhancement in τ_R leads to an increase in r_1. These findings inspired us to further investigate the impact of Cu^{2+} on the r_1 performance of **BHGd** in the presence of HSA at physiological concentrations. As illustrated in Figure 1f, the r_1 of **BHGd** exhibited a slight increase in the presence of HSA alone, which may be attributed to weak interaction between HSA and **BHGd**. Strikingly, upon the addition of 1 eq Cu^{2+} and 0.6 mM HSA, the r_1 of **BHGd** significantly increased from 14.43 ± 0.12 to 18.70 ± 0.16 mM^{-1} s^{-1} (a 29.6% increase). These results suggest the formation of a ternary complex (**BHGd-Cu-HSA**), which restricts molecular rotation and consequently enhances the r_1 of **BHGd**. Furthermore, the phantom experiments demonstrated a significant enhancement in T_1 weighted MR signal intensity upon addition of both Cu^{2+} and HSA (Figures 1g and S7).

Study of High Specificity and Selectivity of BHGd to Cu^{2+}. Next, the specific recognition capability of **BHGd** for Cu^{2+} was characterized using PA imaging and r_1 measurements. As illustrated in Figures 2a,b, S8, and S9, **BHGd** showed a remarkable enhancement in the PA signal at 680 nm exclusively in the presence of Cu^{2+}. Notably, physiological concentrations of competing cations (Mg^{2+}, Ca^{2+}, Fe^{3+}, Zn^{2+}) exhibited no significant interference with the PA signal of **BHGd**, further validating its high specificity for Cu^{2+}. The experimental results demonstrated that **BHGd** exhibited a significantly higher binding affinity for Cu^{2+} compared to other metal ions under solvent conditions (0.1 M HEPES buffer, pH

https://doi.org/10.1021/acs.analchem.5c03093
Anal. Chem. XXXX, XXX, XXX−XXX

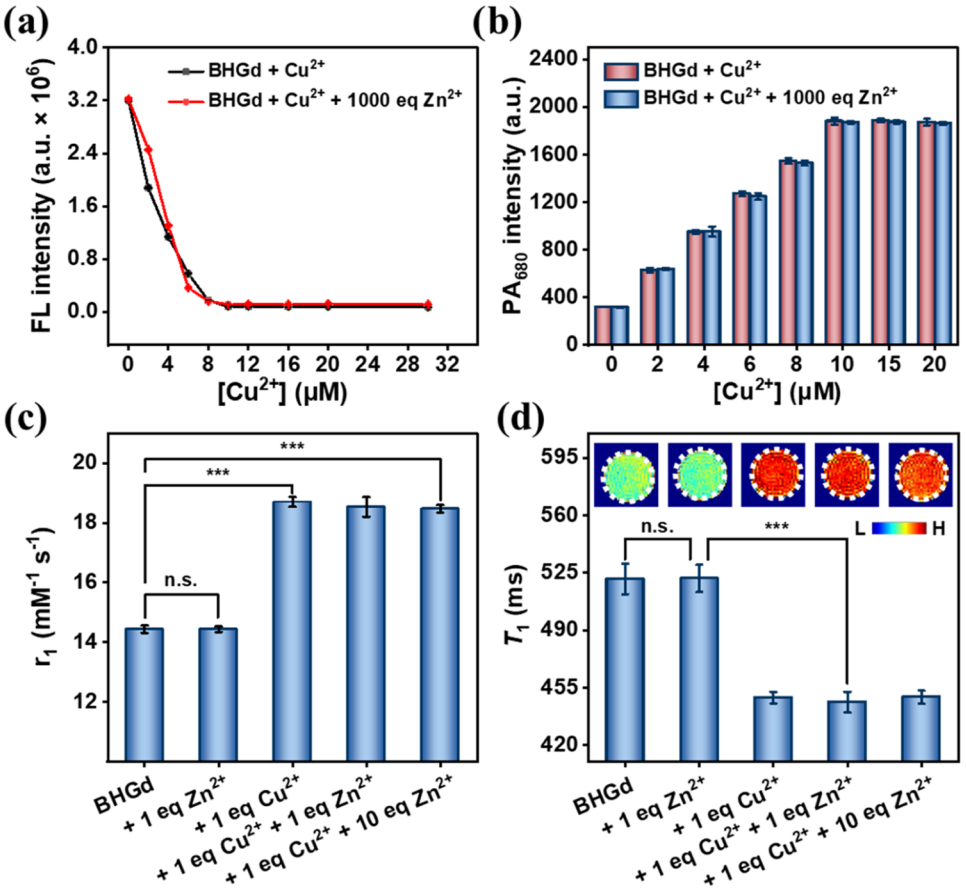

Figure 3. (a) Evolution of fluorescence intensity and (b) PA intensity of **BHGd** in the presence of 1000 eq of Zn^{2+} (vs Zn^{2+}-free control) at varying Cu^{2+} concentrations. (c) Measurements of r_1 for **BHGd** with Cu^{2+} (in the presence of 0.6 mM HSA) at different Zn^{2+} concentrations (1 eq and 10 eq of Zn^{2+}). (d) Corresponding T_1 changes and representative MR phantoms (inset) of **BHGd** (0.3 mM, with 0.6 mM HSA) acquired at 9.4 T under different Zn^{2+} conditions (1 eq and 10 eq of Zn^{2+}). Data represent mean ± SD (n = 3), ***P < 0.001 and n.s., P > 0.05.

7.4). This discovery significantly advanced our investigation into the r_1 of **BHGd** in the presence of various metal ions with or without HSA at physiological concentrations (Figures 2b,c and S10−S12). Upon the addition of Cu^{2+}, the r_1 of **BHGd** increased by 29.6%, while no significant changes were observed for its complexes with Mg^{2+}, Ca^{2+}, Fe^{3+}, or Zn^{2+}. Meanwhile, the MR phantom images of **BHGd** with different metal ions ± HSA were acquired using 9.4 T MR imaging scanner (Figures 2a−e and S13). For other biologically relevant metal ions including Mg^{2+}, Ca^{2+}, Fe^{3+}, and Zn^{2+}, the phantom imaging signal remained unchanged despite variations in their concentrations. These data confirmed that the MR signal of **BHGd** was specifically enhanced in the presence of Cu^{2+}.

A key challenge in the development of Cu^{2+} sensors is their poor selectivity, particularly the difficulty in achieving high specificity to distinguish Cu^{2+} from Zn^{2+}. To address this challenge, we systematically investigated the specific response of **BHGd** to Cu^{2+} in the presence of high concentrations of Zn^{2+} using a multimodal approach combining fluorescence spectroscopy, PA imaging, and r_1 measurements. As shown in Figures 3a,b and S14, the fluorescence signal of **BHGd** at 718 nm progressively decreased, while the PA signal at 680 nm significantly increased upon the gradual addition of Cu^{2+}, even in the presence of 1000 eq of Zn^{2+}. Notably, the variations in fluorescence and PA signals perfectly matched the Cu^{2+} titration profile, demonstrating the high selectivity and binding preference of **BHGd** for Cu^{2+} over Zn^{2+}. Further validation was obtained by r_1 measurements performed in the presence and absence of HSA (Figures 3c and S15). Upon Cu^{2+} addition, r_1 increased from 14.43 ± 0.12 to 18.70 ± 0.16 mM^{-1} s^{-1}, even with a 10 eq of Zn^{2+} as a competing ion. These results confirmed that the binding of **BHGd** to Cu^{2+} in the presence of HSA significantly enhanced r_1, whereas the presence of high concentrations of Zn^{2+} did not interfere with the formation of the **BHGd-Cu-HSA** ternary complex. To further evaluate the selectivity of **BHGd**, T_1 weighted images were acquired at a 9.4 T to assess the impact of Zn^{2+} (Figures 3d and S16). The results demonstrated that **BHGd** displayed exceptional selectivity for Cu^{2+} over Zn^{2+}, as evidenced by the absence of significant changes in image intensity even with 10 eq of Zn^{2+}. Finally, the stability of **BHGd** was systematically evaluated. The results revealed no significant changes in HPLC peak area, PA signal intensity, or T_1 value in DMEM medium supplemented with 10% FBS or across various pH buffers. These findings demonstrated the probe's excellent biological stability and strong potential for application (Figures S17 and S18).

Cellular Study of the Bimodal Probe BHGd upon Cu^{2+} Activation. Before applying **BHGd** in live cell imaging, its cytotoxicity to the MCF-10A cells was assessed using the CCK-8 assay.[37] The results indicated that the viability of MCF-10A cells remained above 85% even at a **BHGd** concentration of 100 μM, demonstrating the high biocompatibility of **BHGd** (Figure 4a). In addition, the cellular uptake kinetics of **BHGd**

https://doi.org/10.1021/acs.analchem.5c03093
Anal. Chem. XXXX, XXX, XXX−XXX

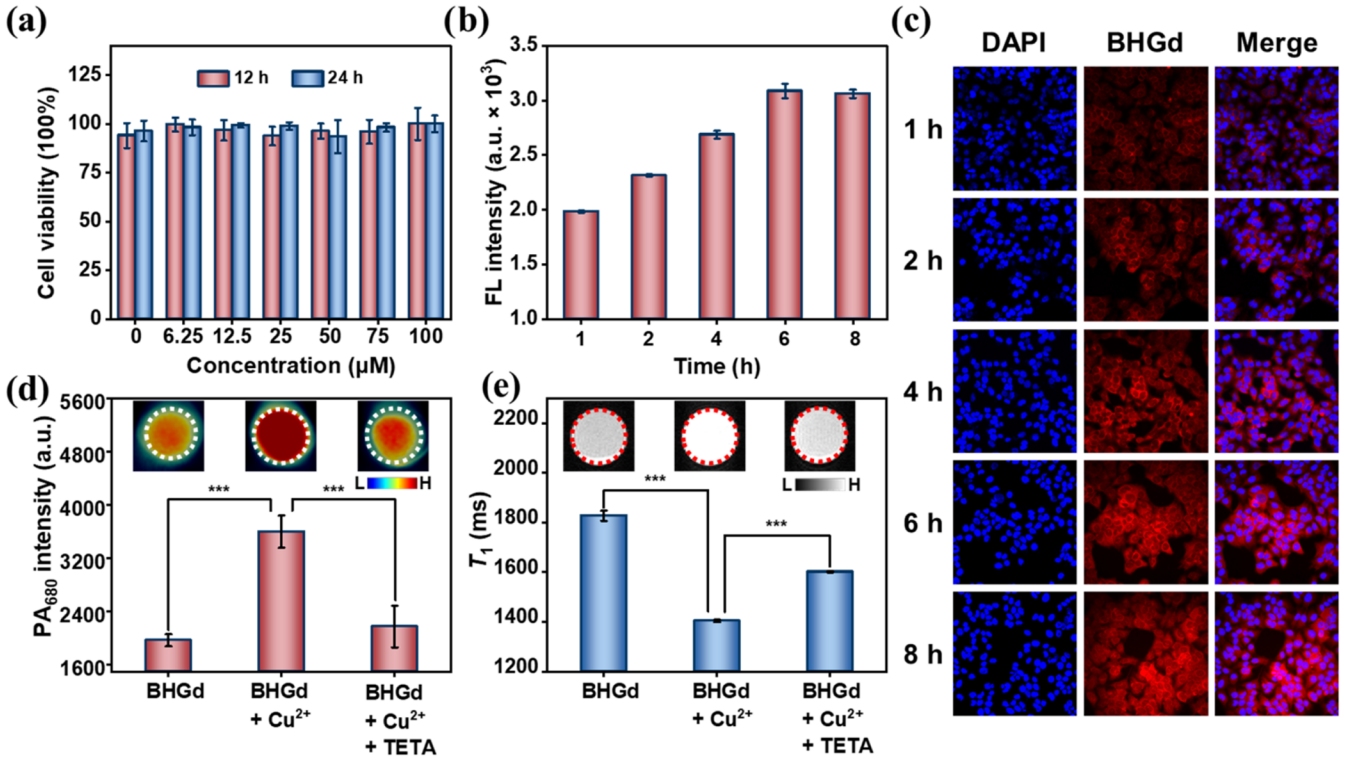

Figure 4. Intracellular labile Cu^{2+} detection using **BHGd**. (a) Cell viability of MCF-10A cells after incubation with various concentrations of **BHGd** for 12 and 24 h, evaluated using the CCK-8 assay. (b) Average intracellular fluorescence intensity and (c) representative time-dependent fluorescence images of MCF-10A cells incubated with BHGd (10 μM) over various time points. (d) Quantification of PA intensity and corresponding PA images (inset) of MCF-10A cell pellets. (e) Quantification of T_1 values and corresponding T_1-weighted images (inset) of MCF-10A cell pellets (at 9.4 T, TE/TR = 5.5:600 ms). Data are presented as mean ± SD (n = 3), ***P < 0.001 and n.s., P > 0.05.

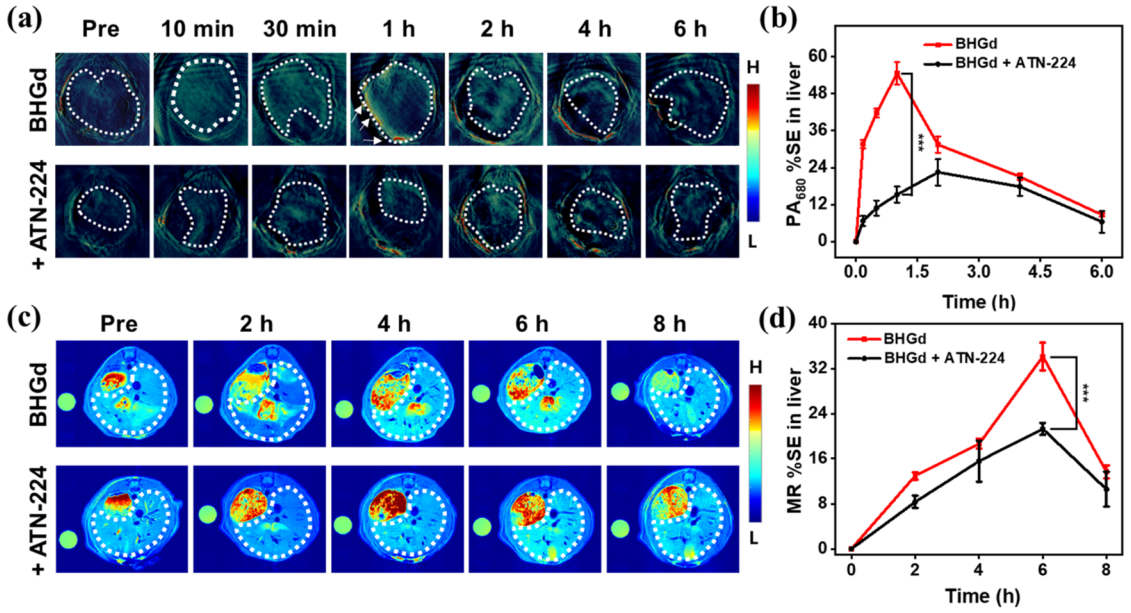

Figure 5. (a) PA images of mouse livers from two groups: **BHGd** (500 μM, 100 μL) and **BHGd** (500 μM, 100 μL) + ATN-224 (5 mg/kg, 50 μL). (b) Percentage PA signal enhancement (%SE) in the livers of mice from different groups. (c) T_1-weighted MR images of mouse livers from the **BHGd** (3.75 mM, 150 μL) and **BHGd** (3.75 mM, 150 μL) + ATN-224 (5 mg/kg) groups. (d) Percentage T_1 signal enhancement (%SE) in the liver of mice from different groups. ATN-224 was administered 2 h prior to **BHGd** injection. Data are presented as mean ± SD (n = 3), ***P < 0.001 and n.s., P > 0.05.

in MCF-10A cells were investigated to optimize the imaging window via synchronized confocal microscopy and flow cytometry. The intracellular fluorescence intensity of **BHGd** progressively increased with incubation time and peaked at 6 h, indicating exceptional membrane permeability (Figure 4b,c). Quantitative analysis obtained through flow cytometry showed high concordance with observations from fluorescence confocal microscopy (Figure S19). These key parameters

https://doi.org/10.1021/acs.analchem.5c03093
Anal. Chem. XXXX, XXX, XXX−XXX

provided a crucial foundation for further research on the detection of Cu^{2+} at the cellular level.

Building on the above result, we investigated the response of **BHGd** to Cu^{2+} *in vitro* using PA imaging and T_1-weighted MR imaging. To elevate intracellular labile Cu^{2+} levels, MCF-10A cells were pretreated with 40 μM Cu^{2+} for 2 h, followed by three washes with PBS (pH 7.4) to remove extracellular Cu^{2+}. The results revealed a 1.7-fold enhancement in PA signal intensity in the Cu^{2+}-treated group, demonstrating the capability of **BHGd** to detect elevated intracellular Cu^{2+} concentrations with high sensitivity (Figure 3d). Notably, pretreatment with the high-affinity Cu^{2+} chelator TETA completely abolished the PA signal enhancement, providing conclusive evidence for copper-dependent **BHGd** activation.[38,39] Complementing the PA imaging results, we performed T_1-weighted MR imaging at 9.4 T to assess the potential of **BHGd** in detecting Cu^{2+}. As shown in Figure 3e, the T_1-weighted images of the Cu^{2+}-treated group exhibited significantly higher signal intensity compared to those of the control groups, highlighting the specific responsiveness of **BHGd** to Cu^{2+}. Taken together, **BHGd** serves as a powerful tool for studying intracellular Cu^{2+} homeostasis, facilitating the elucidation of molecular mechanisms underlying Cu^{2+}-associated physiological and pathological processes.

Visualization of Labile Cu^{2+} Pools in Living Mice Using BHGd. We further evaluated the imaging performance of **BHGd** for detecting labile Cu^{2+} dynamics in the liver of mice using PA and MR imaging. As shown in Figure 5a,b, PA imaging revealed a strong hepatic signal in mice administered with **BHGd**, which peaked at 1 h with approximately 60% signal enhancement, followed by a rapid decline after 2 h. In contrast, the control group pretreated with the copper chelator ATN-224 (5 mg/kg) 2 h prior to **BHGd** injection exhibited a delayed PA signal peak at 2 h, with only a 23% enhancement, significantly lower than that observed in the nonchelated group.[40−42] These results demonstrated that **BHGd**-mediated PA imaging enabled real-time monitoring of Cu^{2+} fluctuations in the liver *in vivo*. Additionally, T_1-weighted MR images of the liver were acquired using a 9.4 T imaging system. As shown in Figure 5c, the T_1 signal in **BHGd**-injected mice peaked at 6 h with a 35% enhancement, whereas the ATN-224-treated group exhibited only a 20% enhancement, reflecting reduced contrast due to Cu^{2+} depletion in the liver. These results demonstrated that **BHGd** enabled precise detection of labile Cu^{2+} fluctuations through both PA and MR imaging. Finally, the acute and systemic toxicity of **BHGd** were further evaluated. H&E-stained sections of the major organs (heart, kidney, liver, lung, spleen) were analyzed 24 h postinjection. As shown in Figure S20, no significant organ damage or inflammatory lesions were observed in both control and experimental groups.

CONCLUSIONS

In summary, we have successfully designed and synthesized a highly efficient dual-modal imaging probe (**BHGd**) responsive to Cu^{2+}. **BHGd** exhibits a rapid and selective response to Cu^{2+}, with a 1:1 stoichiometric ratio. Upon Cu^{2+} binding, **BHGd** exhibits a distinct absorbance shift at 680 nm, and both fluorescence and PA signals show a strong linear correlation with Cu^{2+} concentration, achieving an impressive detection limit of 1.1×10^{-7} M. Moreover, **BHGd** forms a stable ternary complex with Cu^{2+} and HSA, significantly enhancing the T_1-weighted MR signal intensity. Notably, it demonstrates outstanding selectivity and strong anti-interference capability, maintaining stable optical and MR responses even in the presence of high concentrations of competing ions such as Zn^{2+}. Leveraging these superior properties, we successfully achieved dual-modal imaging of labile Cu^{2+} in the liver of mice, revealing concurrent enhancements in both PA and MR signals. This work not only presents a novel strategy for *in vivo* metal ion detection but also provides a powerful tool for the early diagnosis, pathological investigation, and therapeutic evaluation of Cu^{2+}-related diseases. These findings represent a significant advancement in metal ion imaging, laying a strong foundation for the development of next-generation molecular probes with enhanced efficiency and specificity.

ASSOCIATED CONTENT

Supporting Information

The Supporting Information is available free of charge at https://pubs.acs.org/doi/10.1021/acs.analchem.5c03093.

Synthetic route of **BHGd**; NMR, MS, and HPLC of intermediates and final products; HPLC and HRMS analysis of **BHGd** in the presence of Cu^{2+}; stability evaluation of **BHGd**; flow cytometry analysis of MCF-10A cells incubated with **BHGd** (PDF)

AUTHOR INFORMATION

Corresponding Author

Shizhen Chen − *State Key Laboratory of Magnetic Resonance Spectroscopy and Imaging, National Center for Magnetic Resonance in Wuhan, Wuhan Institute of Physics and Mathematics, Innovation Academy for Precision Measurement Science and Technology, Chinese Academy of Sciences, Wuhan 430071, P. R. China; University of Chinese Academy of Sciences, Beijing 100049, P. R. China; School of Biomedical Engineering, Hainan University, Sanya 572019, P. R. China;* orcid.org/0000-0002-4883-5790; Email: chenshizhen@wipm.ac.cn

Authors

Zhaoqing Liu − *State Key Laboratory of Magnetic Resonance Spectroscopy and Imaging, National Center for Magnetic Resonance in Wuhan, Wuhan Institute of Physics and Mathematics, Innovation Academy for Precision Measurement Science and Technology, Chinese Academy of Sciences, Wuhan 430071, P. R. China; University of Chinese Academy of Sciences, Beijing 100049, P. R. China*

Lei Zhang − *State Key Laboratory of Magnetic Resonance Spectroscopy and Imaging, National Center for Magnetic Resonance in Wuhan, Wuhan Institute of Physics and Mathematics, Innovation Academy for Precision Measurement Science and Technology, Chinese Academy of Sciences, Wuhan 430071, P. R. China; University of Chinese Academy of Sciences, Beijing 100049, P. R. China*

Sha Li − *State Key Laboratory of Magnetic Resonance Spectroscopy and Imaging, National Center for Magnetic Resonance in Wuhan, Wuhan Institute of Physics and Mathematics, Innovation Academy for Precision Measurement Science and Technology, Chinese Academy of Sciences, Wuhan 430071, P. R. China; University of Chinese Academy of Sciences, Beijing 100049, P. R. China*

Long Xiao − *State Key Laboratory of Magnetic Resonance Spectroscopy and Imaging, National Center for Magnetic Resonance in Wuhan, Wuhan Institute of Physics and Mathematics, Innovation Academy for Precision*

Measurement Science and Technology, Chinese Academy of Sciences, Wuhan 430071, P. R. China; University of Chinese Academy of Sciences, Beijing 100049, P. R. China

Qiao Yu − *State Key Laboratory of Magnetic Resonance Spectroscopy and Imaging, National Center for Magnetic Resonance in Wuhan, Wuhan Institute of Physics and Mathematics, Innovation Academy for Precision Measurement Science and Technology, Chinese Academy of Sciences, Wuhan 430071, P. R. China*

Yue Zhu − *State Key Laboratory of Magnetic Resonance Spectroscopy and Imaging, National Center for Magnetic Resonance in Wuhan, Wuhan Institute of Physics and Mathematics, Innovation Academy for Precision Measurement Science and Technology, Chinese Academy of Sciences, Wuhan 430071, P. R. China*

Yingying Luo − *State Key Laboratory of Magnetic Resonance Spectroscopy and Imaging, National Center for Magnetic Resonance in Wuhan, Wuhan Institute of Physics and Mathematics, Innovation Academy for Precision Measurement Science and Technology, Chinese Academy of Sciences, Wuhan 430071, P. R. China; University of Chinese Academy of Sciences, Beijing 100049, P. R. China*

Maosong Qiu − *State Key Laboratory of Magnetic Resonance Spectroscopy and Imaging, National Center for Magnetic Resonance in Wuhan, Wuhan Institute of Physics and Mathematics, Innovation Academy for Precision Measurement Science and Technology, Chinese Academy of Sciences, Wuhan 430071, P. R. China; University of Chinese Academy of Sciences, Beijing 100049, P. R. China*

Xin Zhou − *State Key Laboratory of Magnetic Resonance Spectroscopy and Imaging, National Center for Magnetic Resonance in Wuhan, Wuhan Institute of Physics and Mathematics, Innovation Academy for Precision Measurement Science and Technology, Chinese Academy of Sciences, Wuhan 430071, P. R. China; University of Chinese Academy of Sciences, Beijing 100049, P. R. China; School of Biomedical Engineering, Hainan University, Sanya 572019, P. R. China;* orcid.org/0000-0002-5580-7907

Complete contact information is available at: https://pubs.acs.org/10.1021/acs.analchem.5c03093

Author Contributions

[‖]Z.L. and L.Z. contributed equally to this work. All authors have approved the final version of the manuscript.

Notes

The authors declare no competing financial interest.

■ ACKNOWLEDGMENTS

This work was supported by the National Natural Science Foundation of China (U21A20392, 82127802, 22404064, 82102125), the Hubei Provincial Natural Science Foundation of China (2023BCB092 and 2023AFB738), and CAS Youth Interdisciplinary Team (JCTD-2022-13).

■ REFERENCES

(1) Shan, D.; Song, J.; Ren, Y.; Zhang, Y.; Ba, Y.; Luo, P.; Cheng, Q.; Xu, H.; Weng, S.; Zuo, A.; Liu, S.; Han, X.; Deng, J.; Liu, Z. *Cancer Commun.* **2025**, *45* (5), 577−607.

(2) Xue, Q.; Kang, R.; Klionsky, D. J.; Tang, D.; Liu, J.; Chen, X. *Autophagy* **2023**, *19* (8), 2175−2195.

(3) Helman, S. L.; Zhou, J.; Fuqua, B. K.; Lu, Y.; Collins, J. F.; Chen, H.; Vulpe, C. D.; Anderson, G. J.; Frazer, D. M. *BioMetals* **2023**, *36* (2), 263−281.

(4) Liao, Y.; Zhao, J.; Bulek, K.; Tang, F.; Chen, X.; Cai, G.; Jia, S.; Fox, P. L.; Huang, E.; Pizarro, T. T.; Kalady, M. F.; Jackson, M. W.; Bao, S.; Sen, G. C.; Stark, G. R.; Chang, C. J.; Li, X. *Nat. Commun.* **2020**, *11* (1), No. 900.

(5) Gromadzka, G.; Tarnacka, B.; Flaga, A.; Adamczyk, A. *Int. J. Mol. Sci.* **2020**, *21* (23), No. 9259.

(6) Krishnamoorthy, L.; Cotruvo, J. A.; Chan, J.; Kaluarachchi, H.; Muchenditsi, A.; Pendyala, V. S.; Jia, S.; Aron, A. T.; Ackerman, C. M.; Wal, M. N. V.; Guan, T.; Smaga, L. P.; Farhi, S. L.; New, E. J.; Lutsenko, S.; Chang, C. J. *Nat. Chem. Biol.* **2016**, *12* (8), 586−592.

(7) Horn, N.; Wittung-Stafshede, P. *Biomedicines* **2021**, *9* (4), No. 391.

(8) Petruzzelli, R.; Catalano, F.; Crispino, R.; Polishchuk, E. V.; Elia, M.; Masone, A.; Lavigna, G.; Grasso, A.; Battipaglia, M.; Sepe, L. V.; Akdogan, B.; Reinold, Q.; Del Prete, E.; Carrella, D.; Torella, A.; Nigro, V.; Caruso, E.; Innocenti, N.; Biasini, E.; Puchkova, L. V.; Indrieri, A.; Ilyechova, E. Y.; Piccolo, P.; Zischka, H.; Chiesa, R.; Polishchuk, R. S. *Nat. Commun.* **2025**, *16* (1), No. 1468.

(9) Więcek, S.; Paprocka, J. *Metabolites.* **2024**, *14* (1), No. 38.

(10) Billings, J. L.; Hilton, J. B. W.; Liddell, J. R.; Hare, D. J.; Crouch, P. J. *J. Neurochem.* **2023**, *167* (3), 337−346.

(11) Zhu, J.; Graziotto, M. E.; Cottam, V.; Hawtrey, T.; Adair, L. D.; Trist, B. G.; Pham, N. T. H.; Rouaen, J. R. C.; Ohno, C.; Heisler, M.; Vittorio, O.; Double, K. L.; New, E. J. *ACS Sens.* **2024**, *9* (6), 2858−2868.

(12) Wang, S.; Sheng, Z.; Yang, Z.; Hu, D.; Long, X.; Feng, G.; Liu, Y.; Yuan, Z.; Zhang, J.; Zheng, H.; Zhang, X. *Angew. Chem., Int. Ed.* **2019**, *58* (36), 12415−12419.

(13) Xie, D.; King, T. L.; Banerjee, A.; Kohli, V.; Que, E. L. *J. Am. Chem. Soc.* **2016**, *138* (9), 2937−2940.

(14) Zhang, L.; Ma, S.; Wang, T.; Li, S.; Wang, L.; Li, D.; Tian, Y.; Zhang, Q. *Anal. Chem.* **2023**, *95* (2), 1635−1642.

(15) An, Y.; Li, L.; Li, L.; Sun, Y.; Li, B.; Wang, P. *J. Hazard. Mater.* **2024**, *465*, No. 133192.

(16) Que, E. L.; Chang, C. J. *J. Am. Chem. Soc.* **2006**, *128* (50), 15942−15943.

(17) Paranawithana, N. N.; Martins, A. F.; Jordan, V. C.; Zhao, P.; Chirayil, S.; Meloni, G.; Sherry, A. D. *J. Am. Chem. Soc.* **2019**, *141* (28), 11009−11018.

(18) Wang, Y.; Wu, H.; Wu, W.-N.; Yu, Y.-P.; Zhao, X.-L.; Xu, Z.-H.; Xu, Z.-Q.; Fan, Y.-C. *J. Lumin.* **2018**, *204*, 289−295.

(19) Shen, J.-X.; Guo, R.; Wang, M.; Zhu, H.; Jiang, H.; Cui, H.; Wang, K. *Anal. Chem.* **2024**, *96* (44), 17800−17806.

(20) Zimmeter, K.; Pallier, A.; Vileno, B.; Sanadar, M.; Szeremeta, F.; Platas-Iglesias, C.; Faller, P.; Bonnet, C. S.; Sour, A. *Inorg. Chem.* **2024**, *63* (49), 23067−23076.

(21) Yu, J.; Martins, A. F.; Preihs, C.; Jordan, V. C.; Chirayil, S.; Zhao, P.; Wu, Y.; Nasr, K.; Kiefer, G. E.; Sherry, A. D. *J. Am. Chem. Soc.* **2015**, *137* (44), 14173−14179.

(22) Yu, Q.; Zhang, L.; Jiang, M.; Xiao, L.; Xiang, Y.; Wang, R.; Liu, Z.; Zhou, R.; Yang, M.; Li, C.; Liu, M.; Zhou, X.; Chen, S. *Angew. Chem., Int. Ed.* **2023**, *62* (46), No. e202313137.

(23) Li, H.; Liu, Y.; Huang, B.; Zhang, C.; Wang, Z.; She, W.; Liu, Y.; Jiang, P. *Anal. Chem.* **2022**, *94* (29), 10470−10478.

(24) Chen, X.; Ren, X.; Zhu, Y.; Fan, Z.; Zhang, L.; Liu, Z.; Dong, L.; Hai, Z. *Anal. Chem.* **2021**, *93* (27), 9304−9308.

(25) Yan, C.; Liu, D.; An, L.; Wang, Y.; Tian, Q.; Lin, J.; Yang, S. *Anal. Chem.* **2020**, *92* (12), 8254−8261.

(26) Zhao, Z.; Zhang, Y.; Fan, Y.; Cui, C.; Guo, Y.; Zhu, J.; Lv, Z.; Li, M.; Chen, Y.; Shi, H. *ACS Appl. Mater. Interfaces.* **2024**, *16* (39), 51783−51797.

(27) Fang, M.; Xia, S.; Bi, J.; Wigstrom, T. P.; Valenzano, L.; Wang, J.; Tanasova, M.; Luck, R. L.; Liu, H. *Molecules* **2019**, *24* (8), No. 1592.

(28) Pan, D.; Caruthers, S. D.; Senpan, A.; Yalaz, C.; Stacy, A. J.; Hu, G.; Marsh, J. N.; Gaffney, P. J.; Wickline, S. A.; Lanza, G. M. *J. Am. Chem. Soc.* **2011**, *133* (24), 9168−9171.

(29) Ge, R.; Lin, M.; Li, X.; Liu, S.; Wang, W.; Li, S.; Zhang, X.; Liu, Y.; Liu, L.; Shi, F.; Sun, H.; Zhang, H.; Yang, B. *ACS Appl. Mater. Interfaces* **2017**, *9* (23), 19706−19716.
(30) Fanali, G.; di Masi, A.; Trezza, V.; Marino, M.; Fasano, M.; Ascenzi, P. *Mol. Aspects Med.* **2012**, *33* (3), 209−290.
(31) Gao, T.; Yang, S.; Cao, X.; Dong, J.; Zhao, N.; Ge, P.; Zeng, W.; Cheng, Z. *Anal. Chem.* **2017**, *89* (18), 10085−10093.
(32) Hureau, C.; Eury, H.; Guillot, R.; Bijani, C.; Sayen, S.; Solari, P. L.; Guillon, E.; Faller, P.; Dorlet, P. *Chem. - Eur. J.* **2011**, *17* (36), 10151−10160.
(33) Fu, M.; Zhang, L.; Killeen, R.; Onugwu, K. E.; McCarrick, R. M.; Hagerman, A. E. *Molecules* **2025**, *30* (2), No. 320.
(34) Jordan, M. V. C.; Lo, S. T.; Chen, S.; Preihs, C.; Chirayil, S.; Zhang, S.; Kapur, P.; Li, W. H.; De Leon-Rodriguez, L. M.; Lubag, A. J. M.; Rofsky, N. M.; Sherry, A. D. *Proc. Natl. Acad. Sci. U.S.A.* **2016**, *113* (37), E5464−5471.
(35) Martins, A. F.; Jordan, V. C.; Bochner, F.; Chirayil, S.; Paranawithana, N.; Zhang, S.; Lo, S. T.; Wen, X.; Zhao, P.; Neeman, M.; Sherry, A. D. *J. Am. Chem. Soc.* **2018**, *140* (50), 17456−17464.
(36) Srivastava, K.; Ferrauto, G.; Harris, S. M.; Longo, D. L.; Botta, M.; Aime, S.; Pierre, V. C. *Dalton Trans.* **2018**, *47* (33), 11346−11357.
(37) Wang, Z.; Geng, T.; Yue, X.; Zheng, Z.; Zhang, W.; Pan, Z.; Zhang, Q.; Shi, X. *Anal. Chem.* **2025**, *97* (4), 2367−2374.
(38) Soma, S.; Latimer, A. J.; Chun, H.; Vicary, A. C.; Timbalia, S. A.; Boulet, A.; Rahn, J. J.; Chan, S. S. L.; Leary, S. C.; Kim, B.-E.; Gitlin, J. D.; Gohil, V. M. *Proc. Natl. Acad. Sci. U.S.A.* **2018**, *115* (32), 8161−8166.
(39) Lu, X.; Chen, X.; Lin, C.; Yi, Y.; Zhao, S.; Zhu, B.; Deng, W.; Wang, X.; Xie, Z.; Rao, S.; Ni, Z.; You, T.; Li, L.; Huang, Y.; Xue, X.; Yu, Y.; Sun, W.; Shen, X. *Adv. Sci.* **2024**, *11* (18), No. e2309984.
(40) Wang, Z.; Zhang, Y.; Zhang, W.; Gao, H.; Zhong, M.; Huang, T.; Guo, R.; Liu, N.; Li, D.; Li, Y.; Wang, Z.; Zhao, P. *J. Pineal Res.* **2018**, *65* (3), No. e12502.
(41) Doñate, F.; Juarez, J. C.; Burnett, M. E.; Manuia, M. M.; Guan, X.; Shaw, D. E.; Smith, E. L. P.; Timucin, C.; Braunstein, M. J.; Batuman, O. A.; Mazar, A. P. *Br. J. Cancer* **2008**, *98* (4), 776−783.
(42) Lowndes, S. A.; Sheldon, H. V.; Cai, S.; Taylor, J. M.; Harris, A. L. *Microvasc. Res.* **2009**, *77* (3), 314−326.

https://doi.org/10.1021/acs.analchem.5c03093
Anal. Chem. XXXX, XXX, XXX−XXX